Eur. Phys. J. B **48**, 449–462 (2005)
DOI: 10.1140/epjb/e2006-00012-6

THE EUROPEAN PHYSICAL JOURNAL B

Ion-beam induced changes in magnetic and microstructural properties of thin iron films

G.A. Müller, E. Carpene[a], R. Gupta[b], P. Schaaf, K. Zhang, and K.P. Lieb[c]

II. Physikalisches Institut and Sonderforschungsbereich 602, Universität Göttingen, Friedrich-Hund-Platz 1, 37077 Göttingen, Germany

Received 8 July 2005 / Received in final form 20 October 2005
Published online 19 January 2006 –

Abstract. Changes in magnetic and structural properties of 60–82 nm iron films induced by heavy-ion implantation were studied using the magneto-optical Kerr effect, Mössbauer spectroscopy, Rutherford backscattering spectroscopy, X-ray diffraction, and X-ray absorption fine structure. The influence of ion-beam parameters (ion mass, fluence) and of sample parameters (external magnetic field and stress during implantation) were investigated. The Fe films, some of them containing a thin ^{57}Fe marker layer for Mössbauer spectroscopy, were deposited on Si(100) substrates, by electron-beam and effusion-cell evaporation. The films were irradiated with ^{20}Ne, ^{56}Fe, ^{86}Kr and ^{132}Xe ions at energies chosen so that the implantation profiles peaked near the middle of the Fe films. The as-deposited films were magnetically isotropic and had a high coercivity. After ion implantation, the coercivity decreased and magnetic anisotropy developed. Both changes correlated with a decrease in the internal film stress. External mechanical stress applied during the irradiation had hardly any influence on the magnetic texture, opposite to an external magnetic field applied during or before ion implantation. The results are compared with those obtained for ion-irradiated polycrystalline Ni films and epitaxial Fe films and discussed with respect to the role of radiation-induced extended defects as pinning centers.

PACS. 61.72.-y Defects and impurities in crystals; microstructure – 61.82.Bg Metals and alloys – 68.55.Ln Defects and impurities: doping, implantation, distribution, concentration, etc. – 75.30.Gw Magnetic anisotropy – 75.50.Bb Fe and its alloys

1 Introduction

Ion-beam irradiation is a very efficient tool to modify the magnetic properties of thin ferromagnetic films and multilayered structures [1,2]. Hence, work on this topic is not only of fundamental scientific interest, but may lead to attractive technological applications. Several mechanisms are known to be responsible for ion-induced modifications of ferromagnetic films. One important mechanism is ion-beam mixing as demonstrated in the case of Co/Pt multilayers irradiated with He ions [3–5] and Co/Fe multilayers irradiated with Xe ions [6]. In both cases, a reduction in the out-of-plane coercivity was found, opening the possibility for generating magnetic nanostructures by ion-beam writing. Another mechanism is based on producing anisotropic in-plane stress during ion-beam-assisted deposition of Fe or Ni films under the impact of a noble-gas ion beam impinging at inclined incidence relative to the normal direction of the sample [7,8]. Here, an in-plane magnetic anisotropy was induced by inverse magnetostriction. Ion-induced magnetic patterning of exchange-biased thin films is still another recent technique, where ion beams are used to modify magnetic properties [9].

The present work forms part of a comprehensive investigation of the magnetic textures in thin films of 3d-ferromagnetic elements and alloys (permendur, permalloy), induced by heavy-ion irradiation [10–17]. In all these materials, changes in the in-plane magnetic anisotropy and coercivity have been found upon noble-gas and/or metal-ion bombardment. In the case of nickel films, the orientation of the easy axis of magnetization can be influenced by applying an external magnetic or mechanical stress field during the implantation [10–13]. In thin cobalt films, an ion-induced phase transformation from hexagonal to face-centred cubic structure has been observed [16]. However, up to now the underlying causes of this behaviour have not been fully understood. In particular, no mechanism is evident which allows one to predict the orientation of the magnetic texture generated in the

[a] *Present address*: Dipartimento di Fisica, Politecnico di Milano, Piazza Leonardo da Vinci 32, 20133 Milano, Italy.
[b] *Permanent address*: Institute of Instrumentation, Devi Ahilya University, Indore, 452017 India.
[c] e-mail: plieb@gwdg.de

Table 1. Layer structures and ion irradiation conditions.

Sample name	Layer 1 (nm)	Layer 2 (nm)	Layer 3 (nm)	Irradiation parameters
Series A	^{nat}Fe: 75(3)	—	—	Ne, 35 keV, $\Phi \leq 2.5 \times 10^{16}/\mathrm{cm}^2$; External magnetic field $H = 104$ Oe.
	^{nat}Fe: 75(3)	—	—	Fe, 90 keV, $\Phi \leq 5 \times 10^{16}/\mathrm{cm}^2$; 104 Oe.
	^{nat}Fe: 82(3)	—	—	Kr, 130 keV, $\Phi \leq 5 \times 10^{16}/\mathrm{cm}^2$; 104 Oe.
	^{nat}Fe: 82(3)	—	—	Xe, 200 keV, $\Phi \leq 5 \times 10^{16}/\mathrm{cm}^2$; 104 Oe.
M	^{nat}Fe: 23	^{57}Fe: 13	^{nat}Fe: 23	Xe, 200 keV, $\Phi = 1 \times 10^{16}/\mathrm{cm}^2$; Bending $\|\|\varphi = 0°$.
S	^{nat}Fe: 4	^{57}Fe: 13	^{nat}Fe: 41	Xe, 200 keV, $\Phi = 1 \times 10^{16}/\mathrm{cm}^2$; Pre-magnetization by 300-Oe field $\|\|\varphi = 100°$

absence of any magnetic or stress field during implantation at normal ion-beam incidence (no symmetry breaking).

Several materials properties make iron films very attractive for a detailed study of ion-beam-induced magnetic anisotropy. Firstly, polycrystalline Fe films have a very small magnetostriction constant. This is in contrast to the previously studied nickel, cobalt and permendur films, where inverse magnetostriction appears to make the largest contribution to the observed anisotropies. If magnetostriction is less important, it may be possible to isolate contributions from other mechanisms, such as radiation defects. Secondly, the study on iron enables the use of conversion electron Mössbauer spectroscopy (CEMS) using the ^{57}Fe content in the film or ^{57}Fe markers. With a modification of the traditional CEMS technique called magnetic orientation Mössbauer spectroscopy (MOMS [18,19]), one is able to determine the orientation of the in-plane spin distribution. An important advantage of MOMS in comparison to e.g. the magneto-optical Kerr effect (MOKE) is the absence of any external magnetic field during the measurements, which may change the ion-induced magnetization. Thirdly, heavy-ion implantation in iron is known to produce a much smaller defect density as compared to other ferromagnetic metals investigated [20–22]. The density, shape and orientation of these defects are believed to decisively influence the magnetic properties.

For these reasons, it appears challenging to study iron films having different defect structures, either as a consequence of the ion implantation itself or by way of sample deposition. In this work a wide selection of ions ranging in mass from Ne to Xe and in fluence from 1×10^{15} to 5×10^{16} ions/cm^2 was studied. While the polycrystalline films deposited by electron-beam evaporation had a large intrinsic tensile stress, films prepared epitaxially on MgO substrates by pulsed laser deposition (PLD) feature columnar growth and a small compressive intrinsic stress [23,24]. A recent study of ion-beam induced changes of such epitaxial Fe films, indeed, showed a quite different defect structure and no ion-induced magnetic anisotropy [24]. We finally mention recent comparative studies on 350 MeV ^{197}Au^{26+}-ion irradiation of Ni/Si and Fe/Si bilayers [25], which deal with changes of magnetic properties in the regime of electronic stopping.

2 Experiments

2.1 Sample preparation

Series A contains 28 polycrystalline iron films of natural isotope composition (^{nat}Fe), 10×7 mm^2 in size and about 75 or 82 nm thick, which were prepared on Si(100) wafers by electron-gun evaporation. The substrates were mounted at a distance of 26 cm from the gun and not cooled during the deposition. The film thickness was controlled online by a quartz oscillator and later-on by Rutherford backscattering spectroscopy (RBS). The base pressure in the deposition chamber was better than 4×10^{-8} mbar. The magnetic field during deposition was 0.82 Oe, having a 0.62 Oe component along the film plane.

Series B comprises two Fe films, which were prepared in order to investigate the influence of pre-magnetization and external stress on the magnetic anisotropy. The 10×7-mm^2, 60-nm thin iron films were deposited in the centre of 40×15 mm^2 Si(100) wafers. In addition to the ^{nat}Fe layers prepared by e-gun evaporation, both films contained a thin ^{57}Fe marker layer with an isotope enrichment of 95%, located either at the surface (label S) or in the middle (label M) of the layer structure. The ^{57}Fe markers were deposited by an effusion cell. Since the effusion cell and e-gun were mounted in a common vacuum chamber with a base pressure of 4×10^{-8} mbar, the specimens were never exposed to air during the deposition process. The thickness of the marker layer was controlled on-line by a precalibrated flux meter. For a summary of all the samples see Table 1.

2.2 Ion irradiations

All the ion irradiations were carried out at room temperature at the 530-kV Göttingen ion implanter IONAS [26]. For the ^{nat}Fe samples of series A, an external magnetic

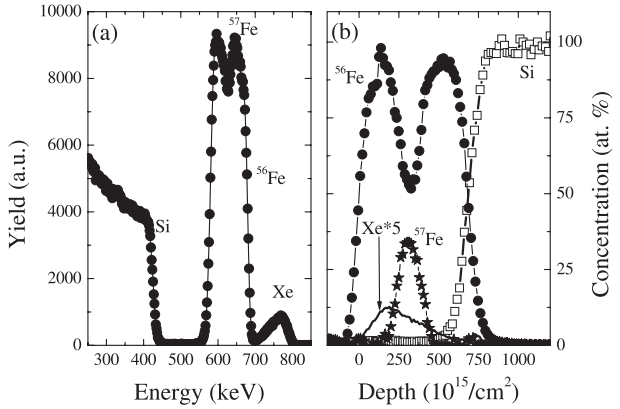

Fig. 1. (a) RBS spectrum and (b) deduced depth profiles of sample M after irradiation with 200 keV Xe-ions at a fluence of 1×10^{16}/cm^2.

field of $H_{\rm impl} = 104$ Oe was applied in the $\varphi = 0°$ direction, which indicates the long axis of the rectangular specimens. The samples were irradiated using beams of ^{20}Ne$^+$, ^{56}Fe$^+$, ^{84}Kr$^+$ and ^{132}Xe$^+$ ions. In order to optimize the magnetic texturing effects, as previously found in the Ni + Xe case [12,13], the projected range of the ion beams was kept at $R \approx 33$ nm, i.e. at about half the film thickness as simulated by SRIM2003 [27]. This required different ion energies: 35 keV Ne, 90 keV Fe, 130 keV Kr and 200 keV Xe. The ions were swept over an area of 10×10 mm^2, homogeneously covering the whole film surface, and the ion current was kept between 0.8 and 1.0 μA in order to avoid sample heating. The ion fluence ranged from $\Phi = 1 \times 10^{15}$ to 5×10^{16} ions/cm^2, the highest fluence in the Ne series was 2.5×10^{16} ions/cm^2.

The implantation conditions for the samples M and S of series B were different. Here we used only Xe ions at the fixed fluence of 1×10^{16}/cm^2 and energy of 200 keV (see Tab. 1). In sample M, a mechanical stress of $\sigma = 57(6)$ MPa was applied by bending the substrate wafer to a curvature of 1 m^{-1}. The bending radius was controlled before and after irradiation by a surface profiler [12,14]. This film was then irradiated in bent condition. The flat sample S was pre-magnetized in the $\varphi = 100°$-direction before the irradiation in an external field of 300 Oe, leaving it in a magnetized state during the ion bombardment.

2.3 Sample characterization

After deposition, the film thickness and layer structure were analyzed by means of RBS using the 900 keV α-particle beam of IONAS. The depth profiles of the various isotopes were deduced from the RBS spectra by means of the WiNDF-program [28]. The RBS analyses were repeated after the ion irradiations. Figure 1a illustrates the capability of RBS to separate the signals from ^{56}Fe and ^{57}Fe, whose concentration profiles are given in Figure 1b; Table 1 summarizes the layer structures. Apart from sputtering (up to 15 nm for the highest Xe-ion fluence), no changes were noted. This is in agreement with the ion energies chosen, which avoided ion-beam mixing at the Fe/Si interface.

The films containing ^{57}Fe markers were analyzed by means of CEMS and MOMS [18,19,29]. These measurements were carried out with a ^{57}Co source of 1–2 GBq activity, which was embedded in a Rh-matrix and driven by a constant acceleration drive. The specimens were mounted in a gas-flow proportional counter, filled with a He + 6%CH_4 mixture. The resulting emission spectra were fitted with superimposed Lorentzian line shapes. Up to three sextets and typically one doublet were required to obtain consistent and good fits of the CEMS data. For each sextet i the hyperfine field $B_{\rm HFi}$, the area fraction F_i, the relative intensities of the sextet components I_{ni} ($n = 1$–6) and the line widths w_j were adjusted. The isomer shifts $\delta_{\rm i}$ and quadrupole splittings Δ_i were set to zero for all the sextets. The velocity axes and isomer shifts were calibrated relative to pure α-iron foils: $B_{\rm HF1} = 32.9$ T, $\Delta_1 = 0$ mm/s. Besides the substitutional, defect-free fraction F_1, the two smaller hyperfine fields can be attributed to substitutional Fe sites with neighbouring lattice defects (mostly vacancy clusters).

In the CEMS geometry, the photon beam entered along the normal direction of the sample, which coincided with the centre axis of the cylindrical conversion electron detector. For the MOMS experiments the specimen normal was tilted 45° away from the incident γ beam and the spectra were measured at different sample rotations φ. In this way, the in-plane spin distribution was obtained from the intensity ratio $I_{21}(\varphi)/I_{31}(\varphi) \equiv I_2/I_3$ of the second and the third lines of the unperturbed α-Fe sextet $i = 1$. As confirmed with MOKE, nearly all the samples had a uniaxially anisotropic magnetization after ion implantation, but exhibited a second local energy minimum at 90° with respect to the easy axis. Consequently, the hyperfine field deduced from the MOMS data was restricted to two in-plane directions $\Psi_{\rm a}$ for the easy axis and $\Psi_{\rm b} = \Psi_{\rm a} - 90°$ for the hard axis, with the corresponding fractions $c_{\rm a}$ and $c_{\rm b}$. Finally, a small out-of-plane component $c_{\rm op} = 1 - c_{\rm a} - c_{\rm b}$ was considered. In this approximation, the intensity ratio I_2/I_3 is given by [18,19,29]

$$\begin{aligned} I_2/I_3 &= (4/3)c_{\rm op} \\ &\quad + 4c_{\rm a}[1 - 0.5\sin^2(\varphi - \Psi_{\rm a})]/[1 + 0.5\sin^2(\varphi - \Psi_{\rm a})] \\ &\quad + 4c_{\rm b}[1 - 0.5\sin^2(\varphi - \Psi_{\rm b})]/[1 + 0.5\sin^2(\varphi - \Psi_{\rm b})]. \quad (1) \end{aligned}$$

Magnetization curves were measured by means of the longitudinal MOKE [30], using a PCSA ellipsometer [14,31], equipped with a pair of Helmholtz coils to produce a magnetic field of up to 1600 Oe. A sample goniometer allowed the automated measurement of the in-plane anisotropy and coercivity with an angular precision of 0.2°. All angular scans were performed with a step size of either $\Delta\varphi = 10°$ or 20°. The coercive field $H_{\rm c}$, the relative remanence $M_{\rm r}/M_{\rm s}$ and the magnetization energy $E_{\rm m}/M_{\rm s}$ normalized to the saturation magnetization $M_{\rm s}$ were deduced from the hysteresis loops at each angle, using in

general the equations [32,33]

$$M_r/M_s = R_0 + R_D|\cos(\varphi - \varphi_0)|, \text{and} \quad (2)$$

$$E_m/M_s = K_0/M_s + K_u/M_s \sin^2(\varphi - \varphi_u), \quad (3)$$

and neglecting any component with fourfold symmetry giving rise to a contribution $(K_1/4M_s)\sin^2(2\varphi - 2\varphi_1)$ in equation (3).

The X-ray diffraction analysis was performed in Bragg-Brentano (XRD) or in grazing incidence geometry (GIXRD) with a Bruker AXS D8 Advance diffractometer, using a Cu-K$_\alpha$ source (λ = 1.54 Å) and a LiF single-crystal monochromator. At the grazing angle $\alpha = 2°$, the measured peak positions of the GIXRD spectra were corrected by [34]

$$\Delta(2\theta) \approx \alpha - (\alpha^2 - \alpha_c^2)^{1/2}, \quad (4)$$

where $\alpha_c = 0.384°$ is the critical angle for iron. The GIXRD-scans yielded the positions of the bcc-Fe (110), (200) and (211) reflexes, from which the average out-of-plane lattice constant a_{op} was derived. The change in the measured lattice constant with changing angle $\psi' = \theta - \alpha$, where ψ' denotes the angle between the sample normal and the incident and reflected X-ray bisector, provided information on the in-plane strain and stress in the film [35,36]. This kind of analysis is known as the $\sin^2\psi'$-method. With the lattice constants a_ψ of the (110), (200) and (211) reflexes, the isotropic in-plane stress σ in the film and the hypothetically stress-free lattice constant a_0 can be obtained by using the formula:

$$(a_{\psi'} - a_0)/a_0 = \sigma[\{(1+\nu)/E\}_{hkl}\sin^2\psi' - \{2\nu/E\}_{hkl}]. \quad (5)$$

This expression is valid for thin films with isotropic in-plane stress σ. As a consequence of the (hkl) dependence of the Poisson ratio ν and the Young modulus E, these parameters have to be derived separately for the different (hkl)-values. Knowing the compliance constants of iron films, $s_{11} = 7.64\ (\text{TPa})^{-1}$, $s_{12} = -2.81\ (\text{TPa})^{-1}$ and $s_{44} = 8.71\ (\text{TPa})^{-1}$, the parameters are [37,38]:

$$E_{110} = 223\ \text{GPa}, \quad \nu_{110} = 0.198,$$
$$E_{200} = 175\ \text{GPa}, \quad \nu_{200} = 0.314,$$
$$E_{211} = 198\ \text{Gpa}, \quad \nu_{211} = 0.294.$$

Changes in the structural defects of e-gun-deposited ^{nat}Fe films for increasing ion fluence were also deduced from extended X-ray absorption fine structure (EXAFS) measurements. We selected samples of set A irradiated with Fe^+, Kr^+ or Xe^+ ions at fluences of 1×10^{16} and 5×10^{16} ions/cm^2. These experiments were performed in backscattering geometry at the BM29 beam-line [39] of the European Synchrotron Radiation Facility (ESRF). The data were analyzed with the *VIPER* software [40], using weighted cubic spline functions to simulate the atomic-like absorption coefficient μ_0(E). The Fourier transformation (FT) was performed in the inverse wavelength range 2 Å$^{-1} \le k \le 15$ Å^{-1}, using a Gaussian window centred

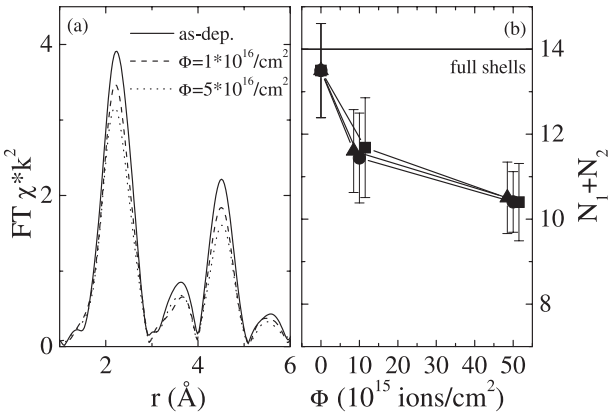

Fig. 2. EXAFS analysis of 75 nm Fe films, as-deposited and after irradiation with 1 and 5×10^{16} Xe-ions/cm^2. (a) Fourier transforms of the quantity χk^2. (b) Variation of the nearest and next-nearest filling numbers, $N_1 + N_2$, with the ion fluence for irradiations with Fe, Kr and Xe ions.

at $k = 8.5$ Å^{-1} and a k^2 weight for the EXAFS spectrum $\chi = [\mu(E) - \mu_0(E)]/\Delta\mu_0$, where the quantity $\Delta\mu_0$ is the typical magnitude of the jump at the absorption edge at E = 7112 eV. The corresponding amplitude and phase were obtained by the simulation and subsequent fit of the calibration sample with the programs *FEFF 8.10* [41] and *FEFFIT 2.55* [42]. A large amount of multiple scattering events prevented the analysis of the higher shells. As the Debye-Waller-factors of all fits of the FT's varied by less than 10%, a constant value was used in all the fits, so that all structural changes refer to the number of nearest and next-nearest neighbours, N_1 and N_2.

The FT's of the Xe-irradiated films, extracted from the product $\chi \cdot k^2$, are shown in Figure 2a. One notes a uniform decrease in signal height for rising ion fluence, which corresponds to a decrease in the coordination number. However, the overall shape of the spectra did not change and no additional peaks correlated to different phases occurred. The parameters resulting from the fitted FT's are the radii R_1 and R_2 of the nearest and next-nearest neighbours and the sum $N_1 + N_2$ of the corresponding coordination numbers. Since R_1 and R_2 differ by only 14% (R_1 = 2.48 Å, R_2 = 2.87 Å), the two peaks overlap strongly in the FT and only the sum $N_1 + N_2$ was deduced from the data as illustrated in Figure 2b and discussed in Section 4.1. The degree of filling the neighbouring lattice sites is expressed by the filling probability, $P_{12} \equiv [N_1(\Phi) + N_2(\Phi)]/14$.

3 Results

3.1 Influence of ion mass and fluence

3.1.1 Magnetic anisotropy

In this section, changes in the magnetic and structural properties of the e-gun-prepared ^{nat}Fe films (series A) induced by the various ions in the presence of an external

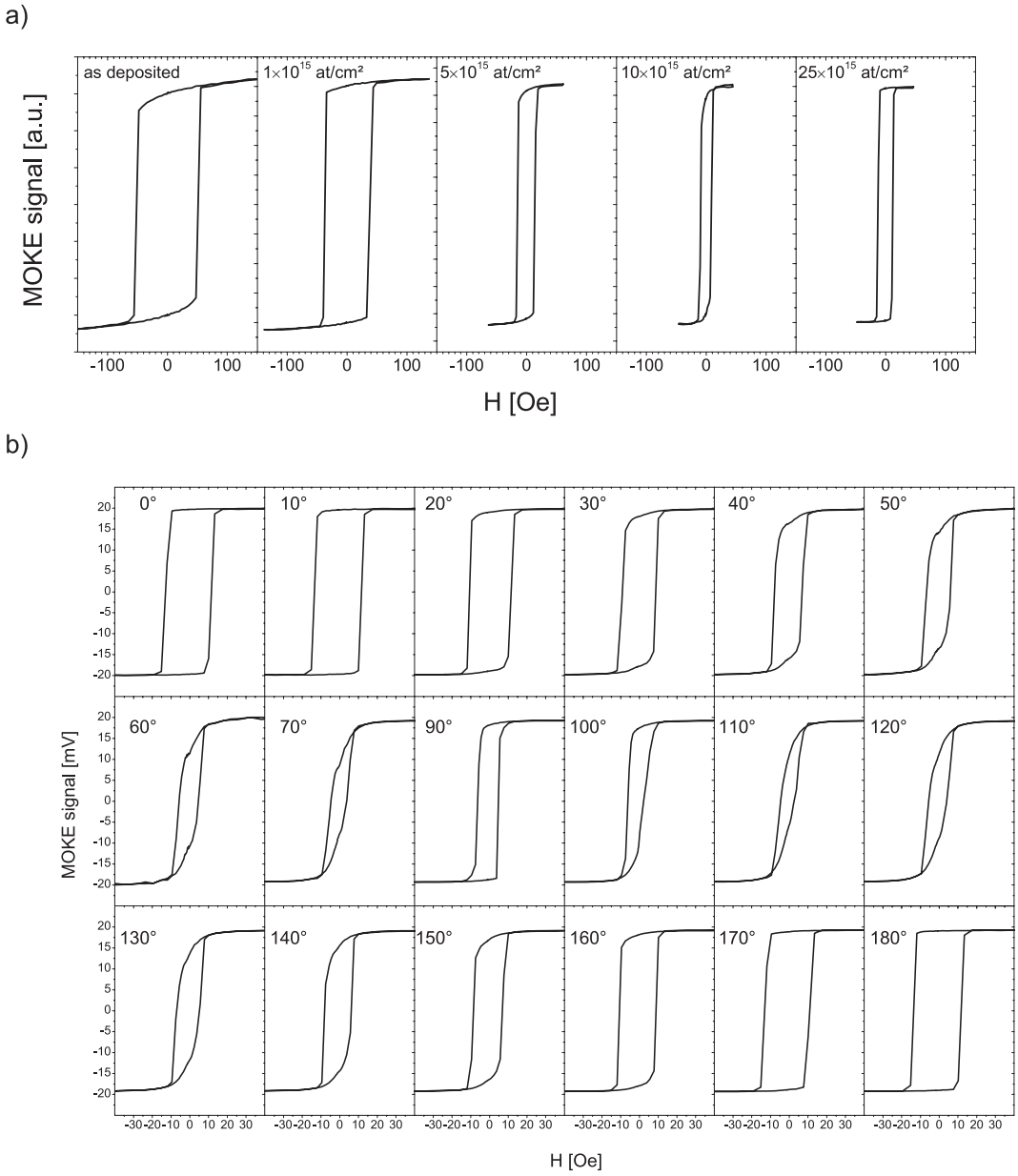

Fig. 3. MOKE hysteresis loops for 75 nm Fe/Si films of set A implanted with 200 keV Xe in an external magnetic field of 104 Oe, which was oriented in the $\varphi = 0^\circ$ direction. (a) Evolution of the hysteris loops at $\varphi = 0^\circ$ as function of the Xe fluence from as deposited to 2.5×10^{16} at/cm^2 (fluences are indicated). (b) Angular variation of the hysteris loops for the sample implanted with 2.5×10^{16} Xe-ions/cm^2 (the angles are indicated).

magnetic field of 104 Oe will be presented. Figure 3 illustrates hysteris loops measured with MOKE before and after ion irradiation for the case of 200 keV Xe ions. Figure 3a illustrates the typical changes for increasing ion fluence, while Figure 3b documents the angular dependence of the coercivity H_c and relative remanence M_r/M_s at the fixed fluence of 1×10^{16} Xe/cm^2, when a full magnetic pattern has developed. The deduced angular scans of H_c and M_r/M_s taken before and after irradiation for the case of 200 keV Xe ions are shown in Figure 4. Both parameters were isotropic after deposition, but showed uniaxial magnetic anisotropy after irradiation, in addition to an isotropic component. The anisotropy rose with increasing ion fluence and was most pronounced at a fluence of $\Phi = 2.5 \times 10^{16}$ Xe-ions/cm^2. In addition to this uniaxial anisotropy, another maximum of M_r/M_s and H_c and a nearly square-shaped hysteresis loop were found perpendicular to the easy axis; triangular hysteresis loops were measured at an interval of 10–20° around this direction. This phenomenon can be interpreted as due to domain blocking in combination with a very small bias field perpendicular to the longitudinal measurement direction [2,43,44]. Thus, to a good approximation, the magnetic anisotropy of the films can be considered uniaxial,

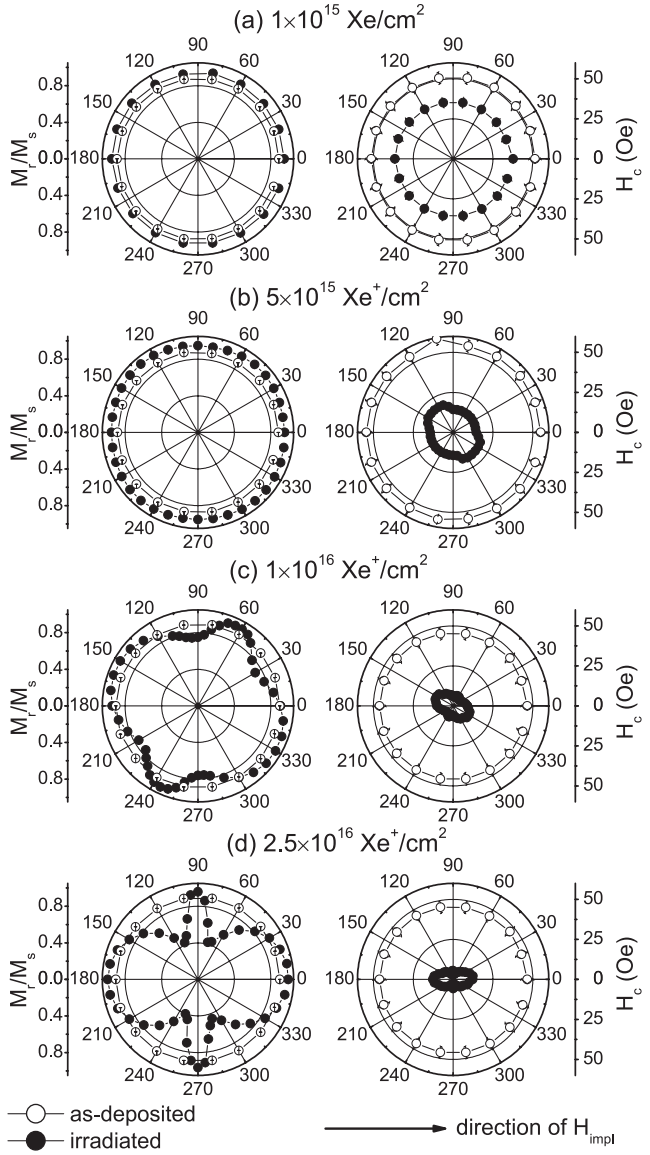

Fig. 4. Variation of coercivity H_c and relative remanence M_r/M_s for iron films irradiated with 200 keV Xe ions in an external magnetic field of 104 Oe, which was oriented in $\varphi = 0°$ direction (MOKE).

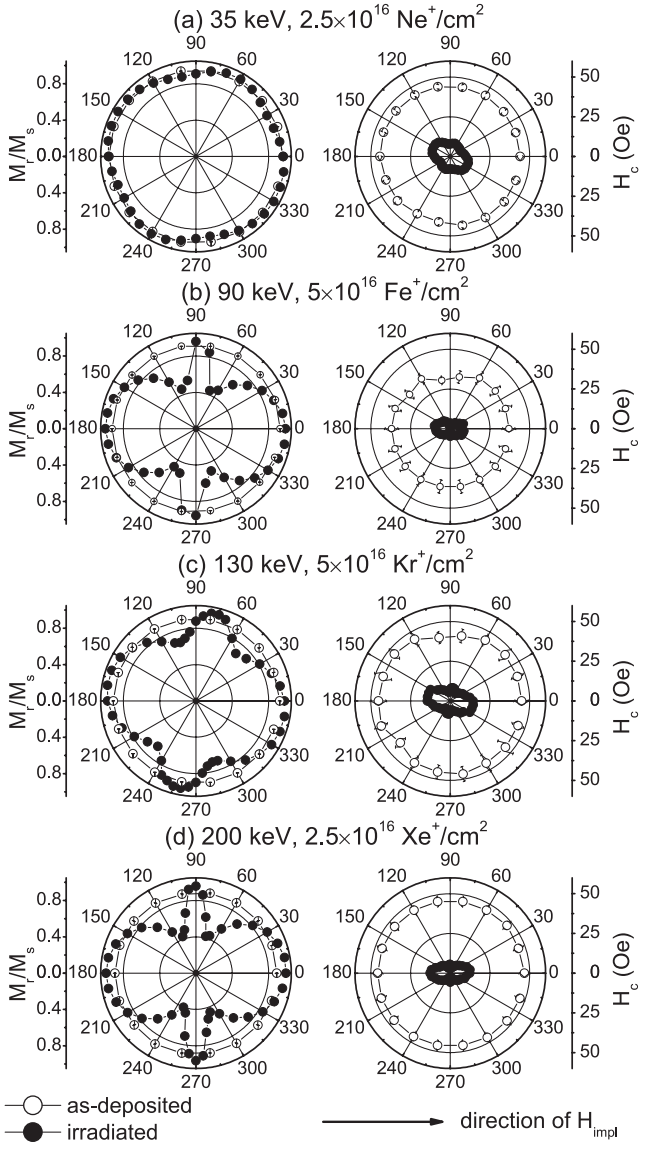

Fig. 5. MOKE polar plots of H_c and M_r/M_s for Ne, Fe, Kr and Xe ions at the fluence, where maximum anisotropy was reached.

with a local high remanence hysteresis in the hard axis direction.

The MOKE polar diagrams obtained for the other ion species Ne, Fe and Kr were similar to the ones presented for Xe. However, the ion fluences necessary to induce the anisotropy with these lighter ions was larger than in the case of Xe. Figure 5 illustrates this observation and summarizes the polar plots at those fluences, which gave the highest anisotropy for each ion species, in most cases $5 \times 10^{16}/\mathrm{cm}^2$. The angular dependence of the magnetization energy $E_m(\varphi)/M_s(\varphi) \equiv E_m/M_s$ was fitted using equation (3) by assuming a superposition of an isotropic part K_0/M_s and a uniaxially anisotropic component K_u/M_s (with its easy axis parallel to φ_u). For the present fits, no fourfold contribution of E_m/M_s was considered [32]. For reasons discussed by Zhang [12], the angles around the hard axis with high values of M_r/M_s and low magnetization energies were excluded from the fits. The resulting parameters K_u/M_s and φ_u are summarized in Table 2 and illustrated in Figure 6.

Because the coercivity in the various as-deposited films was slightly different and the isotropic component of the magnetization energy is closely related to H_c, we introduced the double ratio $\kappa \equiv K_0/M_s(\Phi)/(K_0/M_s)_{\text{as-dep}}$, which pictures the relative change in the isotropic component K_0/M_s due to ion irradiation (see dots in Fig. 6 and Tab. 2). As nearly all the specimens had the same MOKE-saturation signal M_s, the presented values are directly comparable. Only for the highest ion fluence of

Table 2. The values of the parameters κ, (K_u/M_s) and φ_u derived from the MOKE data of series A as function of the ion mass and fluence.

Ion	Φ (10^{15}/cm^2)	κ	K_u/M_s	φ_u (°)
35 keV ^{20}Ne	1.0	0.87(3)	0.55(11)	−19(8)
	2.5	0.87(2)	0.19(8)	43(14)
	5.0	0.63(2)	0.16(17)	20(31)
	7.5	0.62(2)	0.48(16)	5(11)
	10	0.41(2)	0.73(18)	−29(6)
	25	0.25(1)	1.32(15)	−32(4)
90 keV ^{56}Fe	1.0	1.67(17)	≤1.3	30(8)
	2.5	1.10(5)	0.92(32)	28(12)
	5.0	0.33(2)	0.81(18)	−67(8)
	7.5	0.34(2)	0.50(37)	−3(13)
	10	0.23(1)	0.28(15)	−86(18)
	25	0.14(1)	1.81(33)	−5(5)
	50	0.12(4)	4.3(10)	−10(4)
130 keV ^{84}Kr	1.0	0.76(2)	0.60(24)	−46(14)
	2.5	0.47(1)	0.48(23)	59(16)
	5.0	0.19(1)	0.88(24)	0(8)
	7.5	0.11(1)	0.64(13)	15(8)
	10	0.14(2)	1.96(19)	6(4)
	25	0.10(1)	3.1(2)	−6(4)
	50	0.13(3)	4.2(8)	−18(3)
200 keV ^{132}Xe	1.0	1.00(2)	0.19(25)	43(39)
	2.5	0.15(1)	0.90(21)	7(9)
	5.0	0.13(1)	1.18(18)	47(5)
	7.5	0.14(1)	1.94(27)	0(5)
	10	0.13(1)	2.5(3)	35(4)
	25	0.10(2)	4.3(6)	0(3)
	50	0.24(7)	1.97(43)	−30(5)

5×10^{16}/cm^2, the M_s-values were smaller and the resulting anisotropy constants had larger systematic errors.

The following properties of the isotropic component κ are noteworthy:

(i) κ decreased logarithmically with increasing ion fluence and reached a saturation value of $\kappa = 0.15$.
(ii) The decrease in κ depended on the projectile mass. For instance, 2.5×10^{15} Xe ions/cm^2 were sufficient to reach saturation, but for Kr ions the required fluence was 7.5×10^{15}/cm^2 and for Ne ions 2.5×10^{16}/cm^2.
(iii) Although Fe ions have a smaller mass compared with Xe and Kr, the decrease in κ was steeper for them than for Kr and Xe. For a Fe fluence of 1×10^{15}/cm^2 we found $\kappa = 1.7(2)$, i.e. an increase in the isotropic component above the as-deposited value.

The anisotropy parameter K_u/M_s depended on the implanted ion mass and fluence in the following way:

(i) K_u/M_s was very small for small ion fluences, but increased logarithmically with the fluence of the projectiles Fe, Kr and Xe. For Ne only a slight rise was observed.
(ii) The highest Xe fluence induced a slight decrease in anisotropy.
(iii) The increase in K_u/M_s after Fe-ion irradiation started only at 1×10^{16} Fe-ions/cm^2 and not at 5×10^{15}/cm^2 like for the other projectiles.

Concerning the symmetry angle φ_0, good alignment with the direction $\varphi_0 = 0°$ of the external magnetic field was generally found for high fluences and heavy projectiles, but not for the lighter ions and low fluences.

3.1.2 Microstructure

Stress in thin ferromagnetic films has an important influence on their magnetic properties, e.g. inhomogeneously stressed films can develop magnetic anisotropies [38]. Here, one must distinguish between the effects of external mechanical stress, to be discussed in Section 3.2, and those of intrinsic stress, due to film preparation and ion implantation. After deposition the internal tensile stress in a film can be of the order of several GPa [45], depending on the deposition method and material used.

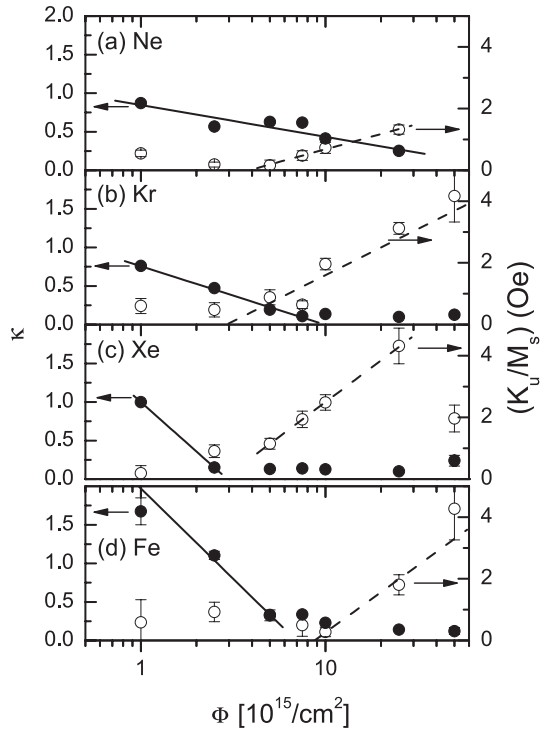

Fig. 6. Fluence dependence of the isotropic part κ (solid symbols) and anisotropy parameter (K_u/M_s) (open symbols) for all four ion species deduced by means of MOKE. The lines are to guide the eye.

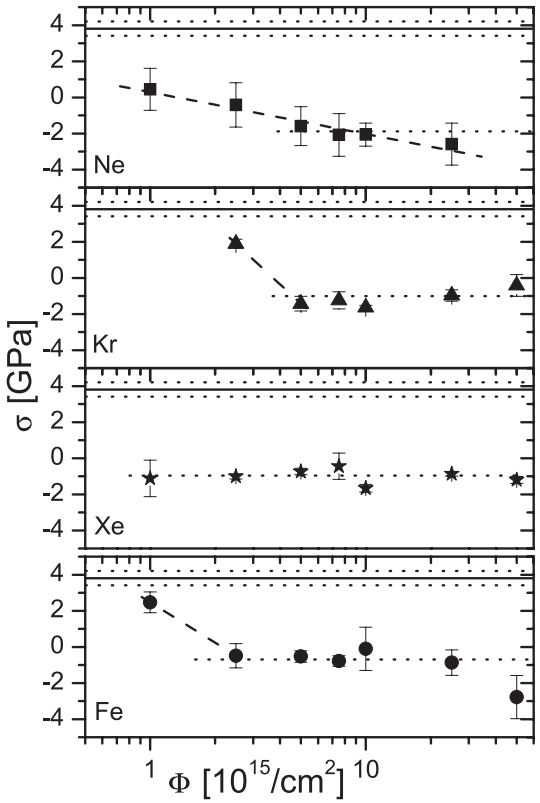

Fig. 7. Fluence dependence of the stress σ for all four ion species, relative to the value in the as-deposited samples, deduced from GIXRD. The horizontal lines indicate the values of σ in the as-deposited films.

The stress σ in the ^{nat}Fe/Si(100) films of series A was analyzed by means of GIXRD as a function of the ion mass and fluence, at a grazing angle of $\alpha = 2°$, as described in Section 2.3. The measured variation of σ with the ion fluence and mass is presented in Figure 7. For rather low fluences, the tensile stress of originally $\sigma = +3.8(4)$ GPa decreased rapidly for any projectile. At a certain ion fluence, which again depended on the ion mass, the stress became zero, turned to be compressive (negative) and finally saturated at $\sigma \approx -1$ GPa, as indicated by the dotted lines. Clearly, the case of Xe is the most extreme one, as the saturation was already reached at only $\Phi = 1 \times 10^{15}/\mathrm{cm}^2$. In the case of Ne^+ projectiles, σ decreased more slowly and continuously and did not reach saturation at the highest fluence of $2.5 \times 10^{16}/\mathrm{cm}^2$.

In Figure 8, the deduced lattice constants a_{op} (circles) and a_0 (dots), defined in Section 2.3 are compared. After deposition, a_{op} was rather small, $a_{op} = 2.865(1)$ Å, and increased with increasing ion fluence, independently of the projectile mass. This behaviour is a consequence of reducing the intrinsic stress in the course of ion implantation. Contrary to this, a_0 in the "stress-free" lattice decreased for low ion fluences of any projectile. For higher fluences, a_0 increased steadily to the saturation value $a_0 = 2.880(1)$ Å, that is close to the value in the as-deposited samples. This increase occurred rapidly for Xe, but slowly for Ne.

The EXAFS data measured after irradiation with Xe, Kr and Fe ions at fluences of 1×10^{16} and 5×10^{16} ions/cm^2

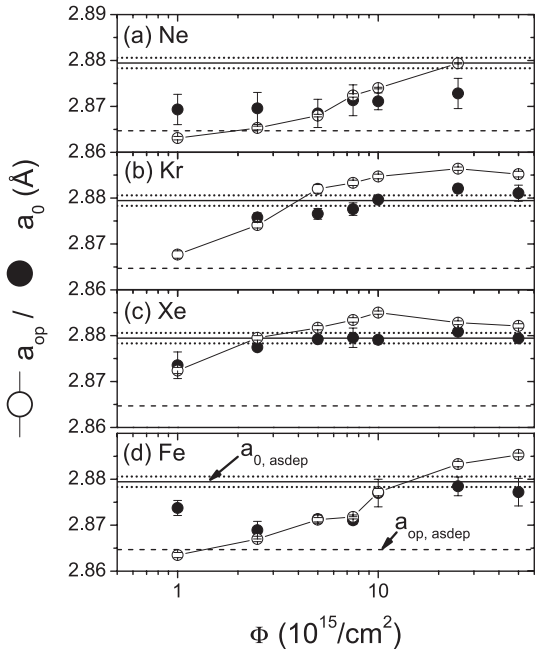

Fig. 8. Fluence dependence of the lattice parameters a_{op} (open symbols) and a_0 (dots) defined in Section 2.3 as deduced from XRD, in comparison with the values in the as-deposited specimens, labelled $a_{0,asdep}$ (solid lines) and $a_{op,asdep}$ (broken lines), respectively.

gave additional information on the short range order in these Fe films. As illustrated in Figure 2b, the filling probability P_{12} decreased in a monotonous and mass-independent manner with increasing ion fluence. In the as-deposited films, the first two shells were nearly completely filled ($P_{12} = 96^{+4}_{-6}\%$), but the filling dropped to 83(6)% for 1×10^{16} Xe-ions/cm^2 and to 75(6)% for 5×10^{16} Xe-ions/cm^2.

3.2 Influence of pre-magnetization and external stress

In the present section, the influence of external conditions during ion irradiation, such as pre-magnetization of the film and external stress, will be discussed. Some preliminary experiments [18] have explored the effects, which external mechanical stress during Xe-irradiation has on the alignment of the magnetic anisotropy in iron films, but no correlation between the stress direction and the easy axis of magnetization has been found, contrary to the results on Ni films [10,12,13]. In these previous experiments on Fe, the specimens were analyzed by means of MOMS and MOKE before and after ion irradiation. As MOKE may have caused some remanent magnetization before irradiation and in order to better distinguish between the effects of pre-magnetization and stress generated by external bending or ion implantation, the order of the analyzing methods applied was now chosen very carefully and will be detailed in each subsection.

3.2.1 Pre-magnetization of the sample S

An important question of magnetic texturing is the "magnetic history" of a sample prior to ion bombardment. In particular, the presence of magnetic fields during film preparation and MOKE analyses of the as-deposited films, possibly leaving them in a pre-magnetized state, may influence the results of subsequent treatments. In this context, the combined or alternative use of MOKE and MOMS was of great advantage, because MOMS is able to determine the hyperfine field(s) in the absence of any external magnetic field, contrary to MOKE (or VSM). The following series of measurements was carried out with sample S: after deposition the sample was analyzed with MOMS, MOKE, RBS and GIXRD (in this order). In the second step, the sample was pre-magnetized with an external field of 300 Oe along the direction $\Psi_a = 100°$, i.e. perpendicular to the symmetry axis determined by MOMS. Thereafter the sample was bombarded with 200 keV Xe^+ ions at a fluence of 1×10^{16}/cm^2 and characterized again in the order MOMS, MOKE, RBS and GIXRD.

The CEM spectra (not shown) were fitted with three sextets and one doublet. The sextets had the hyperfine fields $B_{HF1} = 32.9(1)$ T, $B_{HF2} = 27.3(12)$ T and $B_{HF3} = 19.3(15)$ T, with the corresponding area fractions $F_1 = 85(3)\%$, $F_2 = 7(2)\%$ and $F_3 = 8(3)\%$ after deposition. After irradiation these fractions changed to $F_1 = 70(2)\%$, $F_2 = 13(2)\%$ and $F_3 = 10(3)\%$, indicating a reduction in the coordination number of the iron due to radiation defects. After irradiation, the doublet had a fraction of $F_D = 7(2)\%$, a quadrupole splitting of $\Delta_D \approx 1.1(1)$ mm/s and an isomer shift of $\delta_D = 0.35(6)$ mm/s and originated most probably from oxidation on the film surface.

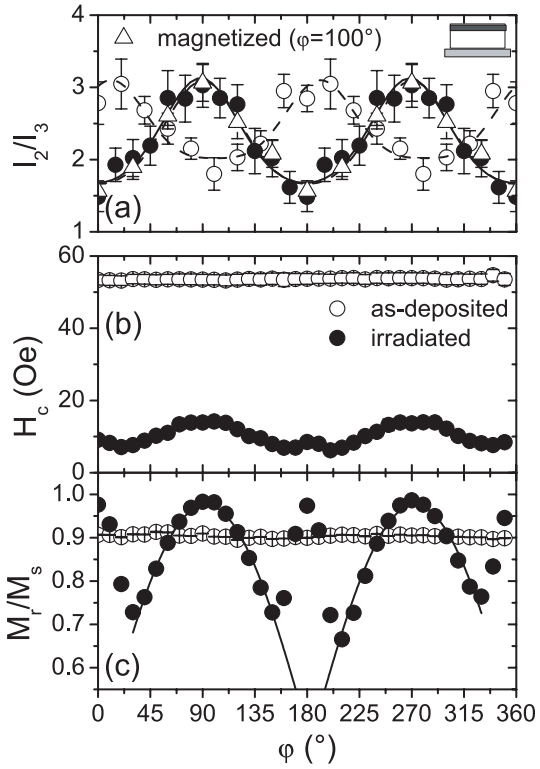

Fig. 9. MOMS and MOKE analyses of sample S. The lines indicate fits with equations (1) and (2). The sketch shows the layer structure with the near-surface ^{57}Fe layer represented in black. (a) MOMS data for the as-deposited, flat sample S (circles) in comparison with those measured after pre-magnetization (triangles) and subsequent Xe-ion irradiation (dots). (b, c) MOKE analyses of the same specimen.

The I_2/I_3 plots of the substitutional, defect-free fraction F_1 measured with MOMS are shown in Figure 8a, for the as-deposited specimen (circles), after pre-magnetization (triangles) and after Xe-irradiation (dots). The corresponding symmetry angles were $\Psi_a = 11(5)°$ after deposition and $\Psi_a = 89(4)°$ after pre-magnetization and ion bombardment. This latter value of Ψ_a was close to that of the pre-magnetizing field, $\Psi_a = 100°$. The amplitude $c_a = 0.66(2)$ of the MOMS oscillation did not change as a consequence of ion bombardment.

Figures 9b and c illustrate the results of the MOKE analyses of this sample. Like in the films of series A, we found square shaped hysteresis loops for the hard axis of magnetization. The in-plane orientation of the easy axis after ion-irradiation was deduced by fitting the uniaxial and isotropic part of the relative remanence M_r/M_s using equation (2). The analyses yielded similar results concerning the magnetic properties as for the samples of series A (see Sect. 3.1). In particular, after deposition H_c and M_r/M_s were isotropic and after irradiation they developed anisotropies, which were very close to those obtained

Table 3. (a) MOMS and CEMS analyses of the samples M and S performed at the various processing steps.

Sample treatment		MOMS				CEMS
	ψ_a (°)	c_a (%)	c_b (%)	c_{op} (%)	c_{op} (%)	
M	as-deposited	49(4)	56(2)	35(2)	8(2)	≤3
	after bending	57(6)	58(2)	42(2)	0	≤7
	after irradiation	58(4)	59(2)	33(2)	8(3)	≤9
	after relaxation	58(4)	59(2)	33(2)	8(3)	≤9
S	as-deposited	11(5)	66(3)	26(3)	8(4)	≤15
	pre-magnetized	90(4)	66(2)	12(2)	22(3)	≤9
	after irradiation	88(4)	67(2)	13(2)	20(3)	≤15

(b) MOKE analyses of samples M and S.

Sample treatment		R_0	R_D	φ_u (°)
M	after relaxation	0.39(4)	0.60(5)	47(5)
S	as-deposited	0.90(2)	0.02(2)	61(8)
	after irradiation	0.43(2)	0.54(2)	93(4)

for Xe-irradiated ^{nat}Fe/Si films. Likewise, the MOMS and MOKE oscillations had the same phase: $\varphi_0 = 93(4)°$. However, in the present sample the anisotropy alignment was achieved by just the remanent magnetization $M_r/M_s > 0.9$ of the film, not by applying an external magnetic field during the irradiation. As will be discussed in Section 4, these results establish a close relationship of the ion-beam induced magnetic anisotropy with the collapse and orientation of asymmetrically shaped vacancy loops. If an external magnetic field or a strong remanent magnetization are present during irradiation of a magnetically isotropic specimen, the mobility of the defects will favour anisotropically shaped (non-magnetic) vacancy loops to orient themselves parallel to the magnetization direction. Thus, carrying out a MOKE analysis before irradiation can disturb the original magnetic state of the film and change the direction of the easy axis. All the fitted parameters of the MOKE and MOMS analyses are summarized in Table 3.

3.2.2 External mechanical stress in the sample M

This series of measurements was carried out with the sample M. After the RBS and GIXRD analyses of the as-deposited sample, the spin distribution was measured with MOMS, thus avoiding any possible change in the magnetization by the MOKE field before implantation. The specimen was then bent to a curvature of $1/R \approx 1/m$ [14,15] and the magnetization was again measured by MOMS. In the next step, the film was irradiated with 1×10^{16} Xe-ions/cm^2 of 200 keV, without applying an external magnetic field, and was analyzed again with MOMS in bent condition. Finally, the external stress was relaxed and the sample was characterized by means of MOMS, RBS, GIXRD and MOKE (in this order).

For fitting the CEM spectra, again three sextets and one doublet were used. The sextets had the same hyperfine field strengths B_{HFi} as before, with the corresponding area fractions $F_1 = 90(1)\%$ and $F_2 = F_3 = 4(1)\%$ after deposition and $F_1 = 85(2)\%$, $F_2 = 8(1)\%$ and $F_3 = 4(2)\%$, after irradiation. This indicated a slight reduction in coordination number due to radiation defects. The fraction F_D of the doublet was below 3% in both cases. Figure 9a shows the graphs of the measured and fitted MOMS intensity ratios I_2/I_3. The circles denote the data for the as-deposited and flat film, and the dots those taken after relaxation of the irradiated film. In both cases, the preferred spin direction was oriented along $\Psi_a = 58(4)°$ and the intensity $c_a = 0.59(2)$ was identical within the error.

The MOKE data shown in Figures 10b and c revealed that the Xe-ion irradiation induced uniaxial anisotropy and square-shaped hysteresis loops around the hard axis. The uniaxial anisotropy was close to the preferred spin direction $\varphi_u = 47(5)°$. From this observation, we conclude that the orientation of the anisotropy was determined during the deposition process and preserved during the following treatments (bending of the substrate, ion irradiation and subsequent relaxation).

4 Discussion

4.1 Correlation of structural defects and magnetic anisotropy

The magnetic anisotropy in mono-elemental metallic films has contributions from magneto-crystalline, magneto-elastic and shape anisotropy. In the present work on e-gun-evaporated Fe films (series A), the magneto-crystalline and magneto-elastic components appear to be negligible. This argument was adopted from XRD analyses of Ni films prepared by e-gun evaporation and irradiated with 200 keV Xe ions. A pole figure analysis did not reveal any in-plane texture, which one would expect in the case of a

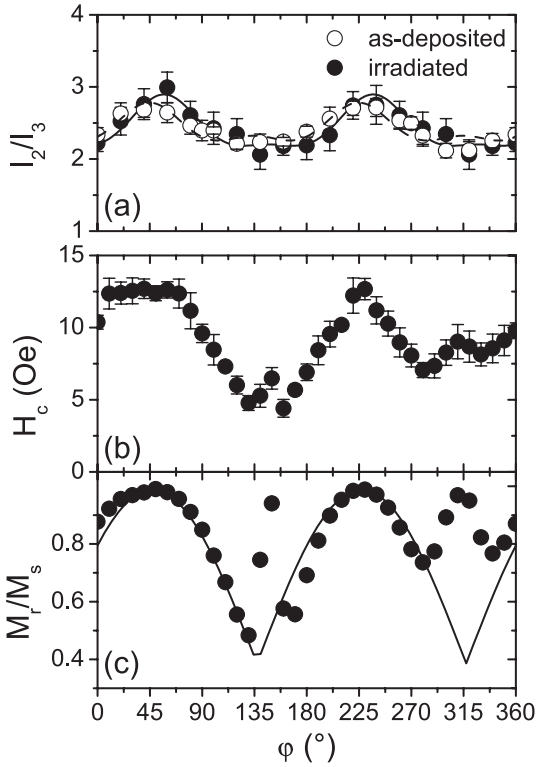

Fig. 10. Same as Figure 9 for sample M. (a) MOMS data for the as-deposited and flat sample (circles) and after irradiation and relaxation (dots). (b, c) Final MOKE analysis after bending, irradiation and relaxation of the sample.

strong magnetocrystalline anisotropy. Furthermore, if the Ni film was stressed inhomogeneously, a GIXRD analysis with the long axis of the film oriented either parallel or perpendicular to the incident X-ray, should yield different diffraction angles. Since the measured GIXRD spectra for both geometries were identical, the anisotropy is not believed to be of magneto-elastic origin.

In analogy with the directional order model for alloys [46], magnetic anisotropy can also be explained by the alignment of vacancies or anisotropic vacancy clusters in the grain boundaries [47]. On the basis of electron micrographs of 30 nm polycrystalline iron films, Antonov et al. [48] proposed a mechanism for the induced magnetic anisotropy by considering the role of vacancy clusters with ellipsoidal shapes. These authors estimated the anisotropy for various concentrations, distributions, eccentricities, and orientations of such vacancy clusters and obtained values for the anisotropy K_u of up to 2×10^5 erg/cm^3.

Obviously, a detailed knowledge of the structural changes induced by ion-beam irradiation is required to understand the various magnetic effects under different conditions of sample treatment and ion beams. In particular, the formation of dislocation loops [20–22] by noble-gas or self-ion irradiation and their interaction with grain boundaries seem to play an important role. The production of dislocations indeed strongly depends on the irradiated material, its crystallographic structure, the projectile mass and the characteristics of the damage cascade. While in bcc-iron films extended defects were found for noble-gas or self-ion fluences exceeding 10^{15} ions/cm^2, comparable defect densities were observed in the fcc-metals nickel or copper at much lower fluences. The collapse of vacancy loops depends on various parameters, among them (i) the defect migration occurring during the thermal spike phase; (ii) the thermal conductivity of the film material; (iii) the cooling rate of the spike region, which is correlated to the melting temperature; and (iv) the initial vacancy configuration and concentration. Irradiation defects in iron are different from those in other metals because here overlapping cascades and, consequently, higher ion fluences are necessary to generate vacancy and interstitial loops, possibly due to differences in the average thermal spike lifetimes [20,22]. For details see the recent work by the Lawrence Livermore-Madrid collaboration [22] and references given there.

The results of the previous sections are in qualitative agreement with the approach of Antonov et al. [48]. As extended defects in iron start to be produced at about 1×10^{15} ions/cm^2 [20], also uniaxial magnetic anisotropy should be visible at this ion fluence and should continue to increase for higher fluences, which is in agreement with the measurements illustrated in Figure 5. Moreover, the efficiency of the vacancy loop formation is supposed to rise with increasing ion mass and, indeed, the anisotropy constant K_u/M_s increased faster for the heavier ions. A quantitative comparison of the measured anisotropy constants with the model of Antonov was made by considering the bulk saturation magnetization for bcc-iron, $M_s = 1711$ emu/cm^3 [49]. Then the largest measured anisotropy constant for 2.5×10^{16} Xe$^+$/cm^2 would be of the order of 4.3 [Oe]$\times$1711 [emu/cm^3] = 7×10^3 [erg/cm^3], corresponding to an extended-defect axis ratio of $a/b \approx 7$, a and b being the typical half-axes of the ellipsoids. A direct observation of the size and orientation of these defect structures may be possible via Transmission Electron Microscopy (TEM).

On the other hand, the presented EXAFS data indicate that the coordination number $N_1 + N_2$ decreased by 17(6)% during irradiation with 1×10^{16} Xe-ions/cm^2 and by 25(6)% during irradiation with 5×10^{16} Xe-ions/cm^2. Within the fairly large uncertainties of $N_1 + N_2$, the reduction did not depend on the ion mass (for Fe, Kr and Xe). Since EXAFS only gives access to the atomic distribution in the crystalline part of the film, it is insensitive to defects at the grain boundaries. However, as the production of dislocation loops depends on the projectile mass [21], we conclude that the defect production responsible for magnetic texturing mainly occurs at grain boundaries. A decrease in grain size, which would affect the EXAFS spectra in a similar way, can be excluded on the basis of the GIXRD results.

A further argument supporting the close connection between the formation of vacancy loops and magnetic anisotropy is based on the fluence dependence of the parameter K_u/M_s in Fe films, as compared with that in Ni or permalloy. In the latter two materials, much lower fluences of some 4×10^{14} Xe/cm^2 were sufficient

to induce magnetic anisotropies [12,13,50]. This observation supports the importance of vacancy loops, whose production in nickel starts at an ion fluence that is one order of magnitude lower than in iron [20].

Besides the ion-induced defects, also the different structural properties of the specimens M and S appear to support the presented explanation. The CEM spectra of samples M and S were fitted with three sextets with hyperfine fields of $B_{\mathrm{HF}} \approx 33$ T, 27 T and 19 T. The lower fields B_{HF2} and B_{HF3} can arise from neighbouring lattice defects such as vacancies or impurity atoms. The area fractions of the defect sites after ion-irradiation were $F_2 + F_3 \approx 15\%$ for M and S. Each vacancy/impurity atom in the nearest neighbourhood of the ^{57}Fe probe nucleus is known to reduce the hyperfine field by 3.6 T [51]. Consequently, the strongly reduced hyperfine fields B_{HF2} and B_{HF3} indicate that these films have a strongly disturbed crystalline structure with a large number of defects (up to four vacancies). On the other hand, the Mössbauer data of a PLD-prepared iron film required only two sextets with $B_{\mathrm{HF}} = 33$ T and 30 T, indicating single-vacancy trapping and the absence of extended vacancy defects [24,51]. In the e-gun samples, the already existing large number of defects is likely to get mobile during ion-irradiation and to collapse to vacancy clusters, while this process does not occur in the PLD films, which have a much smaller defect density after deposition.

4.2 Stress

Two different kinds of stress have been investigated in this work: intrinsic stress due to deposition and/or ion-beam irradiation and external mechanical stress applied by bending the substrate. In the samples of series A, a large intrinsic tensile stress of 3.8(4) GPa was present after deposition; the ion-irradiation with any projectile reduced this value and generated a compressive stress saturating at about −1.0 GPa for the high Fe, Kr and Xe fluences. Similar effects have been found for 150 nm thick Cr films irradiated with 110 keV Ar^+ ions [52], where a fluence of $1 \times 10^{15}/\mathrm{cm}^2$ was sufficient to relax the deposition stress completely. Any further irradiation reversed the (tensile) deposition stress to a compressive stress of −1.0 to −1.5 GPa. This change in stress was explained by the reduction of single voids in the grain boundaries and the net decrease in the interatomic distances in the bombarded films [45,52]. The influence of ion-irradiation induced stress relaxation on the magnetisme of thin films has also been evidenced in EXAFS studies of Devolder and collaborators [3] in a case where practically no stable defects were present. Zhang et al. [13–15] recently discussed the correlation between stress and magnetic polarization in ion-irradiated Ni films. In this system, uniaxial magnetic texture set in at a Xe-ion fluence, where the as-deposited stress vanished. Evidently, similar arguments hold for the interpretation of the fluence dependence of the lattice constant and stress measured in the present work.

The magnetic parameter most sensitive to changes is the coercivity H_{c}, which depends strongly on the defect and grain structure and the internal strains of the specimen [53]. In addition, impurities incorporated during deposition or ion implantation can increase H_{c}. Thus, the high coercivity of the e-gun-deposited films and its strong reduction during the initial stage of irradiation may be explained by the reduction in the intrinsic stress. This argument is supported by our results obtained for PLD-deposited epitaxial Fe-films having a small compressive stress and low coercivity after deposition [24]. The increase in H_{c} after high-fluence ion irradiation, as observed for both types of films, might be correlated to the large number of impurities generating pinning centres in the damage cascades. A similar, but stronger effect has recently been observed by Gupta and collaborators in permendur films irradiated with Xe^+ ions [17,54].

In Xe-ion-irradiated Ni/Si films, external mechanical stress produced by bending or relaxing the substrate strongly influenced the symmetry axis of the uniaxial magnetization [12,13]. This result was obtained by means of MOKE and perturbed γ-ray angular correlations (PAC) with implanted ^{111}In probe ions [55]. However, the present MOMS and MOKE experiments carried out for the bent Fe-sample M gave negative results in the sense that neither bending nor relaxation had an influence on the magnetic texture. The effect on Ni was explained by inverse magnetostriction making a large contribution to the magnetoelastic energy density:

$$E_{\mathrm{me}} = -(3/2)\lambda\sigma\cos^2\varphi, \tag{6}$$

which depends on the magnetostriction constant λ and the stress σ. A comparison of the magnetostriction constants of polycrystalline nickel, $\lambda(\mathrm{Ni}) = -33 \times 10^{-6}$, and iron, $\lambda(\mathrm{Fe}) = -4 \times 10^{-6}$, underlines the importance of magneto-striction in the case of nickel, but to a much lesser extent in iron. We finally mention our recent studies on ion-irradiated permalloy films [50] having a magnetostriction constant $\lambda \approx 0$, where no change in anisotropy due to bending or relaxation was observed, which is in agreement with the results presented here.

5 Conclusions

The present work on ion-beam irradiated polycrystalline iron films, typically 60–82 nm thick and prepared by electron-beam evaporation on Si(100) wafers, aimed at elucidating the influence of several ion beam and sample parameters on the magnetic and microstructural properties, using a combination of X-ray diffraction and absorption, Rutherford backscattering and Mössbauer spectroscopy, and the magneto-optical Kerr effect. The ion-beam parameters investigated were the ion mass and fluence; the effects of magnetic pre-magnetization and external stress were also studied. In all the cases the ion energy was chosen so that the mean ion range was located at about half the film thickness.

The results can be summarized as follows:

(i) For all the samples, the as-deposited films had an almost isotropic magnetization and a coercivity of $H_c >$ 40 Oe.
(ii) For all the ions and for increasing ion fluence, the magnetic anisotropy increased, while the coercivity decreased.
(iii) These changes in the magnetic properties correlated with a relaxation of the tensile in-plane stress after deposition (+3.8 GPa) towards a small compressive stress (−1 GPa) after the implantation at fluences of several 10^{15} ions/cm^2.
(iv) We interpret these findings as due to the formation of extended radiation defects, possibly resulting from built-in defects, which agglomerate under the ion bombardment. On the basis of EXAFS, CEMS and MOKE results, arguments are given that these extended defects are preferentially located at grain boundaries. In particular, the CEM spectra feature large fractions with strongly reduced hyperfine fields, which are typical of highly distorted atomic configurations.
(v) The present results for polycrystalline Fe films are in contrast to those recently gathered for PLD-epitaxially grown films on MgO crystals [24]. Here, the external magnetic field applied during the MOKE analysis before Xe-ion irradiation aligned the magnetocrystalline anisotropy along the (100) easy axis. Any subsequent Xe-ion irradiation had hardly any influence on the magnetic pola-rization. This film exhibited a fourfold anisotropy in MOMS and a twofold anisotropy in MOKE. The ion irradiation caused a decrease in the small compressive stress and a slight increase in coercivity. A similar result was obtained when irradiating FeCo films produced by PLD on MgO crystals with 200 keV Xe ions [50].

Some of the presented results demand further clarification. In particular, Transmission Electron Microscopy may possibly give access to the size and orientation of the extended defects deduced from CEMS and directly verify the differences observed for the electron-evaporated and PLD films. A synopsis of the results obtained after ion implantation into the various ferromagnetic 3d-elements (Fe, Ni, Co) and alloys (permalloy, permendur) is in progress.

The authors wish to thank D. Purschke and A. König for expertly running the IONAS implanter, and Dr. M. Uhrmacher, Dr. M. Münzenberg, Dr. M. Jenkins and the (unknown to us) Referees for fruitful discussions and suggestions. We acknowledge the European Synchrotron Radiation Facility for provision of EXAFS equipment and we would like to thank Silvia Ramos for assistance. The project was supported by Deutsche Forschungsgemein-schaft (DFG) in the frame of SFB 602.

References

1. J. Fassbender, D. Ravelosona, Y. Samson, J. Phys. D **37**, R179 (2004)
2. A. Hubert, R. Schäfer, *Magnetic Domains, The Analysis of Magnetic Microstructures* (Springer, Berlin/Heidelberg, 2000)
3. T. Devolder, S. Pizzini, J. Vogel, H. Bernas, C. Chappert, V. Mathet, M. Borowski, Eur. Phys. J. B **22**, 193 (2001)
4. T. Devolder, C. Chappert, Y. Chen, E. Cambril, H. Bernas, J.-P. Jamet, J. Ferré, Appl. Phys. Lett. **74**, 22, 3383 (1999); H. Bernas, T. Devolder, C. Chappert, J. Ferré, V. Kottler, Y. Chen, C. Vieu, J.P. Jamet, V. Mathet, E. Cambril, O. Kaitasov, S. Lemerle, F. Rousseaux, H. Launois, Nucl. Instr. Meth. B **148**, 872 (1999)
5. C. Chappert, H. Bernas, J. Ferré, V. Kottler, J.-P. Jamet, Y. Chen, E. Cambril, T. Devolder, F. Rousseaux, V. Mathet, H. Launois, Science **280**, 1919 (1998)
6. K. Zhang, R. Gupta, G.A. Müller, P. Schaaf, K.P. Lieb, Appl. Phys. Lett. **84**, 3915 (2004); K. Zhang, K.P. Lieb, M. Marszalek, V. Milinovic, V. Tokman, Appl. Surf. Science, in press
7. M. Farle, H. Saffari, W.A. Lewis, E. Kay, S.B. Hagstrom, IEEE Trans. Magn. **MAG-28**, 2940 (1992)
8. W.A. Lewis, M. Farle, B.M. Clemens, R.L. White, J. Appl. Phys. **75**, 5644 (1994)
9. A. Ehresmann, D. Junk, D. Engel, A. Paetzold, K. Röll, J. Phys. D **38**, 801 (2005)
10. K.P. Lieb, K. Zhang, G.A. Müller, P. Schaaf, M. Uhrmacher, W. Felsch, M. Münzenberg, Acta Phys. Polon. **100** A, 751 (2001)
11. K.P. Lieb, R. Gupta, G.A. Müller, P. Schaaf, M. Uhrmacher, K. Zhang, *Proceedings of the 5th General Conference of the Balkan Physical Union (BPU-5)*, edited by S. Jokic, I. Milosevic, I. Savic (Serbian Physical Society, Belgrade, 2004), pp. 113–134
12. K. Zhang, doctoral thesis, Göttingen (2001); K. Zhang, Nucl. Instr. Methods B, in press
13. K. Zhang, K.P. Lieb, G.A. Müller, M. Münzenberg, P. Schaaf, M. Uhrmacher, Eur. Phys. J. B **42**, 193 (2004)
14. G.A. Müller, doctoral thesis, Göttingen (2003)
15. G.A. Müller, A. Kulinska, K. Zhang, R. Gupta, P. Schaaf, M. Uhrmacher, K.P. Lieb, Hyp. Int. **151/152**, 223 (2004)
16. K. Zhang, R. Gupta, K.P. Lieb, Y. Luo, G.A. Müller, P. Schaaf, M. Uhrmacher, Europhys. Lett. **64**, 668 (2003)
17. R. Gupta, K.-H. Han, K.P. Lieb, G.A. Müller, P. Schaaf, K. Zhang, J. Appl. Phys. **97,** 073911 (2005)
18. G.A. Müller, R. Gupta, K.P. Lieb, P. Schaaf, Appl. Phys. Lett. **82**, 73 (2003)
19. P. Schaaf, G.A. Müller, E. Carpene, in *Mössbauer Spectroscopy in Materials Science*, NATO Science Series, edited by M. Miglierini, M. Mashlan, P. Schaaf (Kluwer Academic, Dordrecht, 2003)
20. M.L. Jenkins, C.A. English, B.L. Eyre, Philos. Mag. **38**, 97 (1978); M.L. Jenkins, M.A. Kirk, W.J. Phythian, J. Nucl. Mat. **205**, 16 (1993)
21. M.A. Kirk, I.M. Robertson, M.L. Jenkins, C.A. English, T.J. Black, J.S. Vetrano, J. Nucl. Mater. **149**, 21 (1987)
22. J.P. Hirth, J. Lothe, *Theory of Dislocations* (Krieger Publishing Co., Malabar, FL, 1982), 2nd edn.; M.J. Caturla, A. Soneda, E. Alonso, B.D. Wirth, T. Diaz de la Rubia, J.M. Perlado, J. Nucl. Mater. **276**, 13 (2000); J. Marian, B.D. Wirth, J.M. Perlado, Phys. Rev. Lett. **88**, 255507 (2002)
23. H.-U. Krebs, Int. J. Non-Equil. Proc. **10**, 3 (1997)
24. G.A. Müller, K.P. Lieb, E. Carpene, K. Zhang, P. Schaaf, J. Faupel, H.-U. Krebs, Hyp. Int. (2005), online

25. V. Milinovic, K.P. Lieb, P.K. Sahoo, P. Schaaf, K. Zhang, S. Klaumünzer, M. Weisheit, Appl. Surf. Science (in press); K. Zhang, K.P. Lieb, V. Milinovic, M. Uhrmacher, S. Klaumünzer, Nucl. Instr. Methods B, in press
26. M. Uhrmacher, K. Pampus, F.J. Bergmeister, D. Purschke, K.P. Lieb, Nucl. Instr. Methods B **9**, 234 (1985)
27. *Stopping Range of Ions in Matter*, SRIM2003 for Windows, `www.srim.org_SRIM_SRIM2003.html`; J.F. Ziegler, J.P. Biersack, U. Littmark, *The Stopping and Ranges of Ions in Solids* (Pergamon Press, New York, 1999), Vol. 1
28. N. Barradas, C. Jeynes, R.P. Webb, Appl. Phys. Lett. **71**, 291 (1997)
29. P. Schaaf, G.A. Müller, E. Carpene, M. Kahle, Hyp. Int. **144/145**, 129 (2002)
30. P.N. Argyres, Phys. Rev. **97**, 334 (1955)
31. R.M.A. Azzam, N.M. Bashara, *Ellipsometry and Polarized Light* (North-Holland, Amsterdam, 1977)
32. M. Brockmann, S. Miethaner, R. Onderka, M. Köhler, F. Himmelhuber, H. Regensburger, F. Bensch, T. Schweinböck, G. Bayreuther, J. Appl. Phys. **81**, 5047 (1997)
33. E.C. Stoner, Proc. Roy. Soc. A **154**, 656 (1936); E.C. Stoner, Proc. Roy. Soc. A **165**, 372 (1938)
34. T. Takayama, Y. Matsumoto, *Advances in X-Ray Analysis*, Vol. 33, edited by C.S. Barrett (Plenum Press, New York, 1990)
35. P.S. Prevey, *Metals Handbook 10* (American Society for Metals, 1986), p. 380
36. M. Jaouen, J. Pacaud, C. Jaouen, Phys. Rev. B **64**, 144106 (2001)
37. J.F. Nye, Physical Properties of Crystals (Oxford University Press, Oxford, 1985)
38. D. Sander, Rep. Prog. Phys. **62**, 809 (1999)
39. A. Filipponi, V.M. Giordano, S. De Panfilis, A. Di Ciocco, E. Principi, A. Trapananti, M. Borowski, Jean-Paul Itiè, Rev. Sci. Instrum. **74**, 2654 (2003)
40. K.V. Klementev, J. Phys. D: Appl. Phys. **34**, 209 (2001)
41. S.I. Zabinsky, J.J. Rehr, A. Ankudinov, R.C. Albers, M.J. Eller, Phys. Rev. B **52**, 2995 (1995)
42. M. Newville, B. Ravel, D. Haskel, J.J. Rehr, E.A. Stern, Y. Yacoby, Physica B **208/209**, 154 (1995)
43. J. Nowak, J. Appl. Phys. **72**, 1490 (1992); J. Nowak, J. Appl. Phys. **73**, 6125 (1993)
44. H.S. Belson, B.F. Desavage, R.S. Tebble, M.R. Parker, IEEE Trans. Magn. **MAG-6**, 722 (1970)
45. J.A. Thornton, D.W. Hoffman, Thin Solid Films **171**, 5 (1989)
46. S. Chikazumi, Phys. Rev. **85**, 918 (1952); S. Chikazumi, J. Phys. Soc. Jpn **10**, 842 (1955)
47. A.G. Lesnik, Phys. Stat. Sol. **35**, 959 (1969); A.G. Lesnik, A.I. Mitsek, V.N. Pushkar, Phys. Stat. Sol. (a) **17**, 697 (1973)
48. L.I. Antonov, V.V. Veter, L.A. Yudina, G.V. Kozodoy, E.L. Fedorova, V.V. Yudin, Fiz. metal. metalloved. **43**, 518 (1977)
49. R. Skomski, J.M.D. Coey, *Permanent Magnetism* (Institute of Physics Publishing, Bristol and Philadelphia, 1999)
50. R. Gupta, K.P. Lieb, G.A. Müller, P. Schaaf, K. Zhang, Hyp. Int., in press
51. M. Neubauer, doctoral thesis, Göttingen (1996); M. Neubauer, K.P. Lieb, P. Schaaf, M. Uhrmacher, Phys. Rev. B **53,** 10237 (1996)
52. A. Misra, S. Fayeulle, H. Kung, T.E. Mitchell, M. Nastasi, Appl. Phys. Lett. **73**, 891 (1998)
53. E. Kneller, *Ferromagnetismus* (Springer-Verlag, Berlin/Göttingen/ Heidelberg, 1962)
54. R. Gupta, G.A. Müller, P. Schaaf, K. Zhang, K.P. Lieb, Nucl. Instr. Methods B **216**, 350 (2004)
55. A. Kulinska, K.P. Lieb, G.A. Müller, M. Uhrmacher, K. Zhang, J. Magn. Magn. Mat. **272–276**, 1149 (2004)